DTU Library

Material classification using basis material decomposition from spectral X-ray CT

Jumanazarov, Doniyor; Alimova, Asalkhon; Abdikarimov, Azamat; Koo, Jakeoung; Poulsen, Henning F.; Olsen, Ulrik L.; Iovea, Mihai

Contents lists available at ScienceDirect

Nuclear Inst. and Methods in Physics Research, A

Full Length Article

Material classification using basis material decomposition from spectral X-ray CT

Doniyor Jumanazarov [a,b,c,d,*,1], Asalkhon Alimova [e,1], Azamat Abdikarimov [a], Jakeoung Koo [f], Henning F. Poulsen [c], Ulrik L. Olsen [c], Mihai Iovea [g]

[a] *Department of Physics, Urgench State University, Urgench 220100, Uzbekistan*
[b] *School of Engineering, Central Asian University, Tashkent 111221, Uzbekistan*
[c] *Technical University of Denmark, DTU Physics, 2800 Kgs. Lyngby, Denmark*
[d] *Department of Telecommunication Engineering, Urgench Branch of Tashkent university of Information Technologies, Urgench 220100, Uzbekistan*
[e] *No. 3 Vocational School, Beshta community, Khazorasp, 220707, Uzbekistan*
[f] *Gachon University, 1342 Seongnam-daero, Sujeong-gu, Seongnam-si, Gyeonggi-do, Republic of Korea*
[g] *ACCENT PRO 2000 s.r.l. (AP2K), Nerva Traian 1, K6, Ap. 26, Bucharest, S3, 031041, Romania*

ARTICLE INFO

ABSTRACT

Spectral X-ray Computed Tomography (CT) exploits advanced photon counting detectors (PCD) to measure a material's spectrally resolved linear attenuation coefficient (LAC) with the simultaneous spectral acquisition at multiple energy thresholds. We present a method for material classification using spectral CT. The method employs a basis material decomposition model and estimates the effective atomic number (Z_{eff}) from the spectral LAC measurements. Basis material decomposition builds on the fact that the LAC of any material can be well approximated by a linear combination of LACs of basis materials, with known Z_{eff} values at the extremes of the relevant Z_{eff} range. Spectral distortions of the energy spectrum due to the physical interactions between photons and the multi-energy-bin PCD such as charge sharing and photon pileup are corrected by a spectral correction algorithm. The validation of the method has been performed with experimental data acquired with a custom laboratory instrument for spectral CT, examining "real life" phantoms with materials in the range of $6 \leq Z_{\text{eff}} \leq 15$. The classification performance is estimated for different numbers of projections, energy bins and basis materials in LAC decomposition. When using just 12 projections, 15 energy bins and two basis materials, the method gives a relative deviation of 2.2% for Z_{eff}, while this deviation is 5.9% when spectral correction is not used. The classification method is now ready for use in security screening where modern spectral CT systems are employed.

1. Introduction

There are different X-ray imaging systems used for material classifications. One is X-ray radiography that measures a line integral of the linear attenuation coefficient (LAC) through an object weighted by the shape of the incoming spectrum, simply called attenuation. Conventional industrial or laboratory based X-ray Computed Tomography (CT) reconstructs the average LAC within an object (human body, airport baggage, etc.) under investigation. This is because the X-ray sources typically produce a polychromatic beam, and conventional CT systems are equipped with energy-integrating detectors for data acquisition, which integrate X-ray photons over a broad energy range and results in the LAC averaged through multiple energies. Material classification from conventional CT is based on the contrast between the averaged LACs of different materials. However, some materials, such as tumor and fibrous tissues [1], soft tissues [2–4] and liquid and homemade explosives [5] may have overlapping averaged LACs, which results in low contrast information and significantly limits the classification performance of single energy CT. Moreover, the extraction of a material's LAC is complicated by polychromatic effects like photon starvation from dense materials or metals [6] and beam hardening [7].

Dual-energy CT has emerged as a better way to minimize these limitations, by probing the LAC of materials at low- and high-energy spectrums and converting them into the energy-independent physical parameters of electron density ρ_e and effective atomic number Z_{eff} [8–11]. Dual-energy CT (DECT) is the state-of-the-art technique for material characterization in medical and security applications [4,9,12–19]. Technically, DECT can be performed in three ways. The first way is rapid kVp switching approach that rapidly modulates the X-ray tube voltage to different kVp levels, generating spectra of lower and higher energies. The second way is by employing energy-sensitive sandwiched detectors with the top-layer and bottom-layer detectors that are superimposed on the other, absorbing lower and higher energy X-ray photons, respectively. The third way is a dual-source CT system with two X-ray tubes and two detectors at an angle of approximately 90° [20–22]. X-ray tubes operating at different tube potential (kV) allow the simultaneous acquisition of dual energy data and the respective applications such as computation of material maps. However, dual-source CT systems have to cope with some challenges, for example, motion artifacts in the two images can be slightly different, which may affect material decomposition. The images therefore need to be co-registered before applying any spectral algorithm. This further increases the complication of the setup.

Quantitative characterization based on ρ_e and Z_{eff} has been found to be highly efficient in security screening [5] and medical diagnosis and radiotherapy [23–27]. Dual-energy CT techniques suffer from the main limitation that low and high energies are overlapping, resulting in low energy separation. Moreover, the performance of these systems is dependent on the selection of the pair of overlapping spectra for data acquisition and the measurement of the spectral responses of the corresponding detectors [28].

To overcome the limitations of dual-energy CT, researchers have recently developed the cadmium telluride (CdTe) photon-counting detectors (PCD) which can discriminate the energy of the detected photons and set up the energy thresholds to assemble and digitize the photon counts. Spectral CT (also known as multi-energy X-ray CT) has emerged as an extension of dual-energy CT, where a single acquisition collects the data in multiple energy bins by using a PCD [29,30]. Spectral CT is able to retrieve a material's LAC at multiple energies and characterize the materials with the presence of K-shell absorption edge in the LAC. It is worth specifying that the limited energy resolution of PCDs induces overlaps between the collected energy bins, which are non-overlapping only in an ideal case. This technique has shown higher potential to improve material separation than dual-energy CT [31] and therefore drawn significant research attention from medical [32–42] and security applications [43,44]. X-ray radiography studies [45–48] also reported that for material characterization PCDs are superior to dual-layer sandwich detectors where the spectral separation is poor.

Decomposing the LACs into multiple components is useful for material classification. Alvarez and Macovski [8] proposed an attenuation decomposition in which the LAC is decomposed into photoelectric absorption and Compton scattering components. Another model is called basis material decomposition that the LAC of any material can be expressed as a linear combination of the LACs of basis materials, typically with very different Z_{eff} values [49–51]. Brambilla et al. [52] showed a material classification method from spectral X-ray radiography acquisition, which estimates material's Z_{eff} based on basis material decomposition. They used MultiX ME100 spectrometric PCD.[2] The method uses a calibration step to register the detector's response for different combinations of thicknesses of the superposed basis materials. They employed polyethylene (PE) and polyvinyl chloride (PVC) as examples of such basis materials. The maximum likelihood function is used to find a superposition of the two basis materials which produces

an attenuation that matches the measured attenuation of unknown materials. From the calculated equivalent thicknesses of basis materials, Z_{eff} of the unknown materials is interpolated or extrapolated. However, from X-ray spectral radiography this method cannot discriminate the materials without information on the sample thickness. Moreover, the estimation accuracy appeared to be low for a thinner and lighter sample behind a thicker and heavier sample, presenting significant limitations [52].

In this work, we adapt the classification method, which was originally proposed by Brambilla et al. [52] for spectral X-ray radiography, to spectral CT system. The spectral CT method can estimate Z_{eff} of materials without knowledge on the sample thickness, and does not depend on location, thickness and density of materials. Experimental data acquired with a custom laboratory instrument is used to evaluate the classification performance, which is tested for different numbers of basis materials in LAC decomposition, energy bins and projections. The method is tested against another spectral CT classification method, named system-independent material classification through attenuation decomposition (SIMCAD) presented in Ref. [53], for identifying/characterizing a wide range of materials.

2. Theory and methods

2.1. Material feature under investigation

For a compound composed of N different elements i each with a number of atoms, α_i, an average atomic number can be calculated and is referred to as the effective atomic number, Z_{eff}, which depends on the atomic numbers of the elements in the compound and on their corresponding quantities. Mayneord (1937) [54] and Spiers (1946) [55] proposed a classical parameterization of Z_{eff}, defined as

$$Z_{eff} = \sqrt[l]{\sum_{i=1}^{N} r_i Z_i^l}, \tag{1}$$

where r_i is the relative electron fraction of each element:

$$r_i = \frac{\alpha_i Z_i}{\sum_{j=1}^{N} \alpha_j Z_j},$$

where α_i is the number of atoms that have the same atomic number Z_i, which also applies to α_j and Z_j. The exponent l is a free parameter that is adjusted depending on the energy range, materials and system features. This exponent typically varies between 2.94 and 3.8 based on experimental fits for various CT systems [51]. Although the atomic number is well defined for chemical elements, there is no single definition of Z_{eff} for any compound. The reader is referred to the reference of Bonnin et al. [56] for a review of different definitions of Z_{eff}. In this work, to be consistent with the previously published works, the exponent l is set to the value of $l = 3.8$ to calculate reference Z_{eff} values of materials scanned and processed.

2.2. Experimental setup and materials

The experiments were carried out in the 3D Imaging Center at DTU, Denmark. The X-ray beam was produced by a micro focused Hamamatsu source of the type L12161–07, with the maximum output power of 75 W. The acceleration tube voltage and the anode filament current were set to 150 kV and 0.5 mA, respectively. The focal spot for these parameters is 75 μm. A 2-mm-thick aluminum filter was inserted in front of the source to suppress photons with energies under the detector's energy range. The incoming beam was collimated to a fan beam by a JJ X-ray IB-C80-AIR slit. Custom built 5-mm-thick tungsten carbide blades in front of the detector decrease photon scattering and fluorescent radiation. The samples were mounted on the rotation stage and scanned between discrete rotations over a range of 360 degrees. The source to detector distance is 701 mm while the source to sample distance is set to 500 mm.

---

[2] This detector is now marketed under the name Detection Technology X-card ME

Table 1

The reference materials used in the calibration step of the classification method. The mass density values ρ for the plastics were estimated with uncertainties of $\pm$ 0.15%. The remaining mass densities are taken from PubChem database [59].

Material	Chemical formula	Width × length/ diameter (mm)	ρ (g/cm^3)	Z_{eff}
Graphite	C	12.7	1.8	6
N,N-Dimethylhydrazine	$C_2H_8N_2$	67	0.791	6.14
Ethylenediamine	$C_2H_8N_2$	67	0.90	6.14
PC	$(CO_3C_{13}H_8)_n$	8.2 × 53.5	1.18	6.48
Acetone 2	C_3H_6O	54	0.785	6.44
Nitrobenzene	$C_6H_5NO_2$	49	1.20	6.68
PMMA	$(C_5O_2H_8)_n$	40 × 42	1.18	6.60
Ethanol 96%	C_2H_6O (96%)	67 × 67	0.798	6.58
Methanol	CH_3OH	20	0.792	6.86
POM-C	$(CH_2O)_n$	9 × 53.5	1.41	7.07
Hydrazine solution	H_4N_2 (35%)	54	1.0	7.24
Nitromethane	CH_3NO_2	20	1.14	7.27
Water	H_2O	20	0.997	7.54
Water 3	H_2O	12.7	0.997	7.54
Hyd. Peroxide 2	H_2O_2 (50%)	73 × 74	1.22	7.65
PTFE	$(C_2F_4)_n$	9 × 53.3	2.16	8.50
Magnesium 2	Mg	18	1.74	12
Aluminum 2	Al	20 × 20	2.70	13

Table 2

The test materials used in the material property calculation step of the classification method. The mass density values ρ for the plastics were estimated with uncertainties of $\pm$ 0.15%. The remaining mass densities are taken from PubChem database [59].

Material	Chemical formula	Width × length/ diameter (mm)	ρ (g/cm^3)	Z_{eff}
2-Butanone	C_4H_8O	83	0.805	6.29
Acetone	C_3H_6O	20	0.785	6.44
PET	$(C_{10}H_8O_4)_n$	9 × 53.5	1.39	6.74
Methanol 2	CH_3OH	81	0.792	6.86
POM	$(CH_2O)_n$	12.7	1.42	7.07
POM-H	$(CH_2O)_n$	15.5 × 53.3	1.43	7.07
Ethanol 40%	C_2H_6O (40%)	67 × 67	0.947	7.19
Water 2	H_2O	51 × 51	0.997	7.54
Nitric acid	HNO_3 (65%)	83	1.39	7.67
Hyd. Peroxide	H_2O_2 (50%)	20	1.22	7.65
PVDF	$(C_2H_2F_2)_n$	9 × 53.5	1.79	8.01
PTFE 2	$(C_2F_4)_n$	12.7	2.2	8.50
Magnesium	Mg	12.7	1.74	12
Aluminum	Al	25	2.70	13
Silicon	Si	12.7	2.33	14

performance as a function of the number of basis materials are given in Section 3.4. In this work, the total exposure time per projection is set to 8 s (i.e. 80 repeated acquisitions are recorded with the integration time of 100 ms and averaged) to obtain all the results, except those presented in Fig. 8(b) and 8(c).

2.3. Data correction and energy bins rebinning

The next steps in the material classification pipeline after data acquisition are data correction and energy bins rebinning. The energy-dependent physical interactions inside the PCD such as (flux-independent) charge sharing, weighting potential cross-talk, fluorescence radiation (escape peaks), Compton scattering radiation and electronic noise, and (flux-dependent) photon pile up and incomplete charge collection severely distort the measured spectra. These effects decrease the detector's energy resolution and lead to large deviations of the extracted LACs from expected values, especially at low and high energies, which in turn significantly decreases material classification performance. The importance of the spectral correction for detector response artifacts in material identification using spectral CT was presented in Ref. [60]. In this work, we therefore use the correction algorithm proposed by Dreier et al. [58] to correct the spectral distortions in the PCD used. The correction algorithm has been implemented successfully in the used PCD for fluxes up to 5 Mph/s/mm^2. The comprehensive semianalytical interpretations based on the physical reason of the different interactions are used for the correction of the measured flat field and attenuated spectra. Since the detector effects are energy and flux dependent, different samples give different spectral distortions, and thus, different errors in their LAC extraction.

Fig. 1 compares the spectral LACs derived from the raw data and data corrected for spectral distortions, exemplified for a water sample. The LAC mean value and respective standard deviation within a region of interest (ROI) are calculated for each energy bin. The correction algorithm shows significant restoration of the distorted LACs towards the reference curve, except for the low and high energies. The reason for this is photon starvation (i.e. complete attenuation of photons) at low energies and low source intensity at high energies. Therefore, the energy bins below the low-energy threshold (E_l = 33.2 keV) and above the high-energy threshold (E_h = 132.4 keV) are excluded in the characterization of materials. The low energy bins have very low photon counts because of the aluminum filter with high absorption which was placed in front of the source. Since the LAC is calculated based on the Beer–Lambert's law to account for X-ray attenuation, a step in the correction algorithm sets the LAC to 0 for the low energy

We use MultiX ME-100 v2 PCD for the experiments, manufactured by Detection Technology S.A.S. in Moirans, France. The detector consists of a system of five detector modules, each module possessing a 1 × 128 linear array of 0.8 × 0.8 mm^2 pixels. The detector captures the incident photons with energies between 20 and 160 keV, which are distributed in 128 energy bins each with a width of 1.1 keV. The detector has an energy resolution of 6.5% (8 keV at 122 keV) at fluxes under 2 Mph/s/mm^2, defined by the Full Width at Half Maximum (FWHM) [57]. The detector is built to perform well at high fluxes (above 10^6 photons/mm^2/s and up to 10^7 photons/mm^2/s) [57,58], while the flat field flux from the source was 1.23 Mph/s/mm^2 in this work. The integration time of the detector ranges between 2 ms and 100 ms (in 10 μs increments).

Table 1 lists the reference materials and Table 2 lists the test materials, which are employed in the calibration and material property calculation steps of the classification method described in Section 2.6. The reference Z_{eff} values shown in the tables are computed by Eq. (1) and the exponent l = 3.8. Sample dimensions are described through width × length for rectangular samples and diameter for circular samples. The plastics are polycarbonate (PC), polymethyl methacrylate (PMMA), polyoxymethylene-C (POM-C), polytetrafluoroethylene (PTFE), polyethylene terephthalate (PET), polyoxymethylene-H (POM-H) and polyvinylidene fluoride (PVDF). These plastics were selected for the characterization because their chemical compositions closely resemble several explosives, e.g. POM can be regarded as an explosive simulant [46]. Z_{eff} values of most organic materials range between 7 and 8 [5]. None of the materials used have absorption edges in the detector's energy range.

The measured raw data undergoes a spectral detector correction briefly described in the next subsection. The results of a classification performance investigation with and without spectral correction are shown in Section 3.1. The samples were mounted on the rotation stage and scanned between discrete rotations with certain increments over a range of 360 degrees. The magnitude of increments is set depending on the number of projections taken during the CT scan. The classification performance is also estimated for different numbers of projections such as 360, 36, 12 and 7, for which the results are given in Section 3.2. This analysis step is followed by an energy bins rebinning into different numbers of bins, exploring the classification performance as a function of the number of bins, for which the results are presented in Section 3.3. Spectral LACs are extracted after image reconstruction step and then undergo basis material decomposition. The results of classification
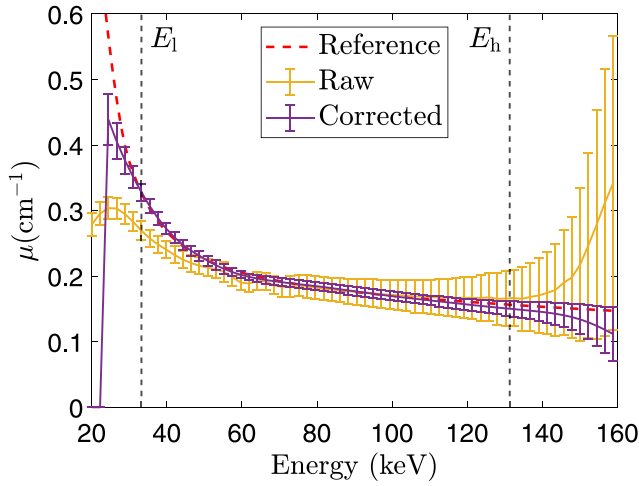
Fig. 1. Spectral LACs extracted from the raw data and data corrected for the spectral distortions, for a water sample. The reference LACs were taken from NIST database [61]. The error-bars represent the respective standard deviation values. The vertical black dash-dotted lines show the low- and high-energy thresholds denoted by E_l and E_h, respectively, which are set to exclude bins in which the LACs cannot be fully restored.

bins to avoid the consequence of NaNs, Infs, and very low counts. Fig. 1 therefore shows the corrected LAC curve with a sharp drop-off around 25 keV.

The energy region is thus truncated to exclude bins for which there is still a large deviation of the corrected LAC from the reference curve, because of incomplete restoration of the original spectrum by the correction algorithm. The energy bins rebinning is performed after the spectral correction step and setting the low- and high-energy thresholds. The rebinning procedure groups together neighboring bins with widths that are considerably smaller than the detector's energy resolution. This will serve a twofold purpose, while preserving the advantages of multiple bins. Firstly, the signal-to-noise ratio (SNR) in each bin is increased since the SNR is proportional to the square root of the expected number of photons [62]. Secondly, the computation time required for image reconstruction decreases linearly with the reduction in the number of bins. Thus, in this work we use cases that reduce the energy bins to 2, 6, 15 and 90 energy bins without and with introduced energy gaps in the spectra. A source spectrum is sampled for the 2 bins case such that the bins are separated by a spectral gap between the boundaries of 60.8 and 69.6 keV. The gap width was selected such that it is slightly larger than the detector's resolution, supposing a constant energy resolution of 8 keV (FWHM) [57], and the gap is approximately at the center of the source spectrum. In the cases of 6 and 15 bins, the bins are uniformly distributed across the spectrum. Independent energy bins with no overlaps are expected to enhance the effectiveness of spectral algorithms. If so, the optimal rebinning should be provided by 6 bins (from 33.2 to 132.4 keV) with 8.8 keV widths and with inter-gaps of 8.8 keV. This configuration, which can be easily adapted to the case of study with discrete bins of width 1.1 keV, should provide the highest number of independent bins. The case of 15 bins has bins with 3.3 keV widths and inter-gaps of 3.3 keV. The 90 bins case involves no rebinning since the number of bins between the low- and high-energy thresholds is equal to 90.

2.4. Reconstruction algorithm and LAC extraction

The next step in the pipeline after data correction and energy bins rebinning is image reconstruction. The results presented in the Sections 3.3 and 3.5 are obtained with filtered backprojection (FBP) and the simultaneous iterative reconstruction technique (SIRT) [63]

algorithms, respectively. The results presented in the other subsections are produced with L_∞ norm-based vectorial total variation (L_∞-VTV) regularization that employs correlations between multiple energy bins. The L_∞-VTV uses a weighting parameter λ between the regularization term and the data fidelity terms, determining the strength of the regularization. The joint regularization term is added to the data fidelity terms to more accurately reconstruct images from noisy or few projections. This regularization norm jointly penalizes the violation of the inter-bin relations, leading to strong couplings between the image gradients over multiple energy bins. The algorithm can therefore efficiently minimize the influence of outliers in the gradient magnitudes. The joint reconstruction thus augments the available data with extra information from other energy bins. The classification performance is explored as a function of λ in this study. More details regarding the L_∞-VTV can be found in Jumanazarov et al. [64].

After the reconstruction is performed, for each energy bin the mean LAC within an ROI is extracted from the LAC histogram which is fitted to a normal distribution. Each ROI is manually segmented in the reconstruction as shown in Fig. 6(a). The reconstruction algorithms used in this work can also be applied to heterogeneous materials. It requires more efforts to segment heterogeneous materials than homogeneous ones, but with the correct segmentation the classification accuracy is expected not to be greatly influenced.

2.5. Basis material decomposition and basis materials used

In X-ray CT, materials are differentiated thanks to their LAC μ. The LAC of any scanned material can be decomposed into a linear combination of LACs of multiple basis materials with respective magnitudes, and this is the so-called basis material decomposition (BMD) model and represented as [49–51,65–67]

$$\mu(E_k) = a_1\mu_1(E_k) + a_2\mu_2(E_k) + \cdots + a_N\mu_N(E_k), \quad (2)$$

where $\mu_i(E_k)$ $(i = 1, 2, \ldots, N; \; k = 1, 2, \ldots, K)$ denotes LAC of the basis material i for the energy bin E_k, with N and K being the total numbers of basis materials and energy bins, respectively. a_i represents an adimensional magnitude without a physical unit for the basis material i.

We reformulate Eq. (2) as a linear system of equations to compute the a_i magnitudes for the basis materials:

$$\begin{pmatrix} \vec{\mu}_1 & \cdots & \vec{\mu}_N \end{pmatrix} \begin{pmatrix} a_1 \\ \vdots \\ a_N \end{pmatrix} = \begin{pmatrix} \mu(E_1) \\ \vdots \\ \mu(E_K) \end{pmatrix} \quad (3)$$

where $\vec{\mu}_i = (\mu_i(E_1), \ldots, \mu_i(E_K))^T$. The number of basis materials cannot be greater than the number of energy bins, otherwise the above system of equations will be under-determined. We employ a linear least square solver called **lsqnonneg** function in MATLAB® with the positivity constraint on the solution, which gives the vector of $(a_1, \ldots, a_N)$ magnitudes that minimizes the norm.

Fig. 2 shows the basis material decomposition of the LACs of a water 2 sample, obtained by using two basis materials, PE and PVC, and 15 energy bins. The plot shows that using Eq. (2) the spectral LACs of the scanned material can be reproduced accurately based on a combination of the LACs of the basis materials computed from Eq. (3).

An unknown material can also be expressed as a linear combination of the two physical contributions resulting from photoelectric absorption and Compton scattering forming a reference basis. With this approach, Alvarez and Macovski [8] originally proposed a method for the discrimination of materials based on atomic numbers and mass densities, which is mainly employed in luggage inspection. The BMD model has an advantage over the photoelectric absorption-Compton scattering model that it can be used to reproduce the spectral LACs of materials with K-edge discontinuities. This could be done by including a basis material that presents a K-edge discontinuity within the energy
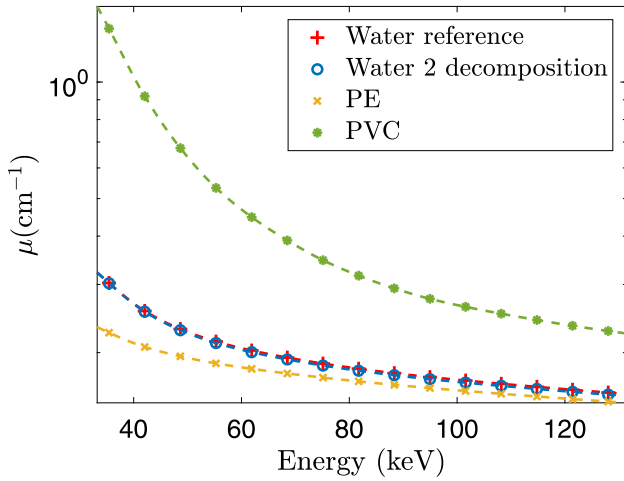
Fig. 2. Basis material decomposition of the LACs of a water 2 sample introduced in Table 2. The LACs of the basis materials, PE and PVC, and reference LACs of water were obtained from NIST database [61]. Note logarithmic scale in the y-axis.
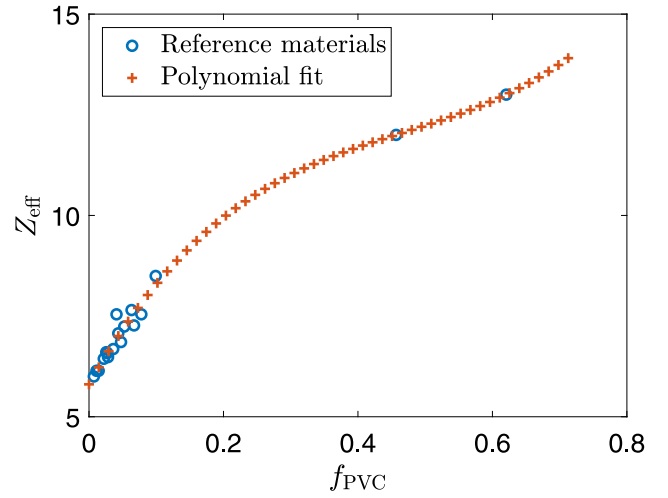

Fig. 3. Z_{eff} values of the reference materials (listed Table 1) as a function of PVC volume fraction defined in the basis material decomposition of LAC, for which PE and PVC are used. The calibration data can be fitted by a polynomial function of degree 3, shown by the red crosses. The plot was reproduced with 15 energy bins.

Table 3
The basis materials used in the estimation of classification performance as a function of the number of basis materials in LAC decomposition. The mass densities are taken from in PubChem data [59].

Basis material	Chemical formula	ρ (g/cm^3)	Z_{eff}
Polyethylene (PE)	$(C_2H_4)_n$	0.93	5.56
Polyacetylene (PAc)	$(C_2H_2)_n$	0.4	5.76
Polypyrrole (PPy)	$(C_4H_5N)_n$	0.97	6.03
Polymethyl methacrylate (PMMA)	$(C_5O_2H_8)_n$	0.94	6.60
Polyoxymethylene (POM)	$(CH_2O)_n$	1.42	7.07
Polyvinyl Chloride (PVC)	$(C_2H_3Cl)_n$	1.406	14.44

Table 4
The basis materials used for the classifications with the different numbers of basis materials in LAC decomposition.

Number of basis materials	Basis materials
2	PE, PVC
3	PE, PPy, PVC
4	PE, PPy, POM, PVC
5	PE, PAc, PPy, POM, PVC
6	PE, PAc, PPy, PMMA, POM, PVC

range of interest, but the use of a basis material for each of the possible K-edge energies may be a necessity [52,68].

The classification performance is also estimated for different numbers of basis materials in the basis material decomposition model. Table 3 introduces the basis materials used to estimate the classification performance as a function of the number of basis materials in the decomposition, i.e. the dimensionality of LAC space. Table 4 tabulates the basis materials used for each of the different numbers of basis materials in the classifications. Note that only theoretical LAC values of the basis materials, taken from the NIST database [61], are used in the classifications. Each classification always uses PE and PVC as the basis materials with the lowest and highest Z_{eff} value in the decomposition, respectively.

2.6. Calibration and calculation of the material property

The next step in the pipeline after LAC extraction and basis material decomposition of LAC is a calibration step in which a set of reference materials is measured and finally calculation of a material's Z_{eff}. A polynomial curve fitting technique can be used for the estimation of Z_{eff} based on X-ray spectral CT acquisition. The so-called volume fraction for the basis material N with the highest Z_{eff} value among the basis materials in the decomposition, denoted by f_N, is a monotonically increasing function of Z_{eff} value of materials. Z_{eff} can be fitted by a polynomial function of degree 3:

$$Z_{eff} = c_0 + c_1 \cdot f_N + c_2 \cdot f_N^2 + c_3 \cdot f_N^3, \qquad (4)$$

where c is a set of polynomial regression coefficients depending on the numbers of basis materials and energy bins in the decomposition, and parameters of the experimental setup, as obvious from Eq. (3). The volume fraction f_N is defined as

$$f_N = \frac{a_N}{\sum_{i=1}^{N} a_i}, \qquad (5)$$

where the magnitudes a_i and a_N, computed by Eq. (3), correspond to the basis material i ($i = 1, 2, \ldots, N$) and basis material N with the highest Z_{eff} value in the decomposition, respectively.

In this work, we apply the polynomial curve fitting technique for the estimation of Z_{eff}, defined in Eq. (4), to spectral CT. Since each classification always uses PVC as the basis material with the highest Z_{eff} value in the decomposition, for the remainder of the paper we denote its volume fraction as f_{PVC}. Fig. 3 illustrates that Z_{eff} value of the reference materials listed in Table 1 indeed monotonically increases with PVC volume fraction in LAC decomposition into the basis materials of PE and PVC. This calibration process of the conversion between the volume fraction and Z_{eff} is needed for further classification of unknown materials, using at least two different basis materials. As this calibration step finds relations between Z_{eff} and volume fractions by using a group of reference materials, Eq. (4) can also be employed to deduce the Z_{eff} values of other materials from the measured volume fraction values, like the test materials tabulated in Table 2. Note that the method will be more accurate for a group of estimated materials within a range of Z_{eff} values of basis materials, otherwise, the estimated PVC volume fraction will be larger than one which may lead to lower accuracy in fitting Z_{eff} through extrapolation.
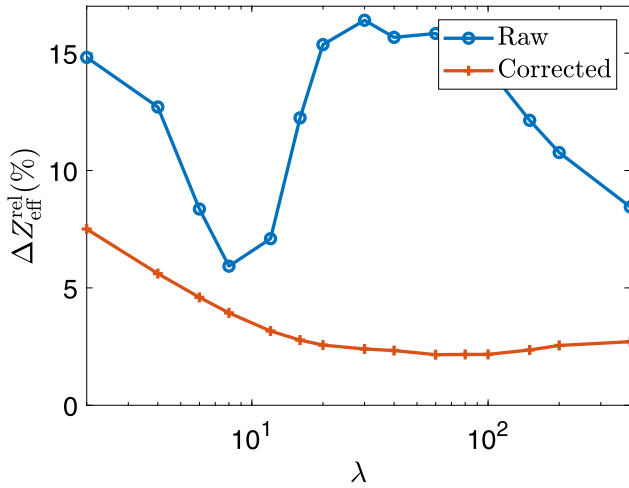
Fig. 4. The relative deviations for Z_{eff} as a function of weighting parameter λ, obtained with the raw and corrected data. The graphs show the mean absolute values of relative deviations calculated from the test materials listed in Table 2. The calibration step was performed using the reference materials listed in Table 1. Corrected data collected from 12 projections and rebinned into 15 energy bins, and PE and PVC as basis materials, were used to obtain the results presented. Note the logarithmic scale in the x-axis.

In this work, the classification performance is estimated as the relative deviation based on the reference values of Z_{eff}, defined as

$$\varDelta Z_{\text{eff}}^{\text{rel}} = 100\% \cdot \frac{Z_{\text{eff}}^{\text{est}} - Z_{\text{eff}}^{\text{ref}}}{Z_{\text{eff}}^{\text{ref}}}, \qquad (6)$$

where superscripts est and ref indicate the estimated and reference values, respectively.

3. Results and discussions

3.1. Classification from the raw and corrected data

As described in Section 2.3, the effect of the spectral distortion degrades the performance of the detector for extracting the spectral LACs, which can largely be recovered by the correction algorithm. Fig. 4 shows how the spectral correction can significantly improve the

classification performance computed as a function of the weighting parameter λ of the L_∞-VTV, which was used in this subsection. The raw data gives the relative deviation of 5.9% (at $\lambda = 8$), while the deviation decreases to 2.2% (at $\lambda = 60$) for the corrected data. Moreover, for raw data the evolution of deviations are not stable with variations in λ. Instead slight changes result in very different deviations for Z_{eff}. The correction for the detector's spectral distortions is thus required for the classification, and therefore we use the corrected data for the estimates presented in the other subsections.

The correction algorithm will work in the same way for higher Z_{eff} materials of interest in medical imaging, such as iodine, calcium, gadolinium or tantalum [58], even though they may have K-edges within the energy range of the X-ray source. The materials tested in this work are relevant to the security applications but also resemble the density and atomic number of organic tissues. Human organs are mostly composed of H, C, N, and O [27], and body tissues change between $6 \leq Z_{\text{eff}} \leq 15$ within the detector's energy region [69–72].

3.2. Evaluation of classification performance for different numbers of projections

We tested the classification performance for different numbers of projections evenly distributed between 0 and 360 degrees. The collection of the projections enables a reconstruction of the sample by using the reconstruction algorithm. To combat the heavy sparse-view artifacts due to the use of decreasing number of projections and improve denoising performance of spectral CT with low SNRs, we use the L_∞-VTV joint reconstruction algorithm in this subsection. Fig. 5(a) shows the mean relative deviations for Z_{eff} as a function of λ for different datasets collected from 360, 36, 12 and 7 projections, with 2.2% (at $\lambda = 1.2$) for 360, 2.0% (at $\lambda = 16$) for 36, 2.2% (at $\lambda = 60$) for 12 and 2.0% (at $\lambda = 1000$) for 7 projections. The relative deviations for different materials corresponding to the optimal λ values are shown in Fig. 5(b). As the number of projections decreases, the optimal λ giving the maximal classification performance increases, because the number of sinogram elements in the data fidelity term for each energy bin decreases while the regularization term is independent of the number of projections (see definitions of the data fidelity and regularization terms for the reconstruction algorithm in Ref. [64]). The optimal range of the weighting parameter therefore appears to be quite different from each other for different numbers of projections.
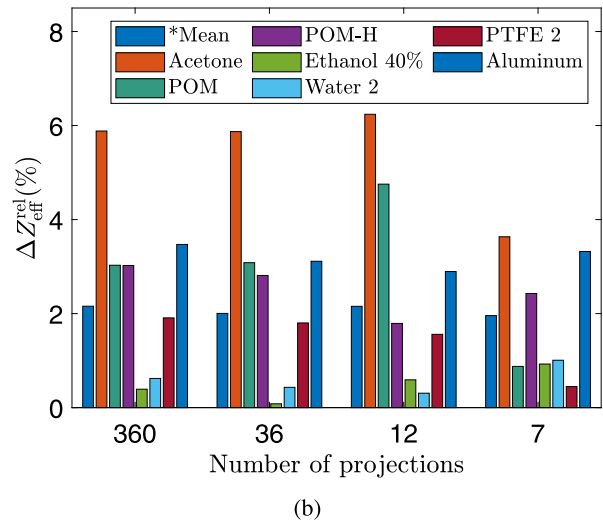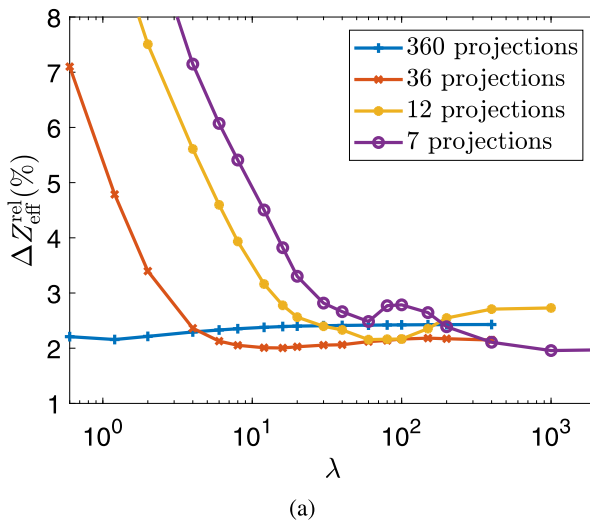

(a)

(b)

Fig. 5. The mean relative deviations for Z_{eff} as a function of weighting parameter λ (a) and relative deviations for different materials (b), obtained with 360, 36, 12 and 7 projections. *The mean deviation was calculated from absolute values of relative deviations for the test materials listed in Table 2. The calibration step was performed using the reference materials listed in Table 1. Corrected data rebinned into 15 energy bins, and PE and PVC as basis materials, were used to obtain the results presented. Note the logarithmic scale in the x-axis in (a).
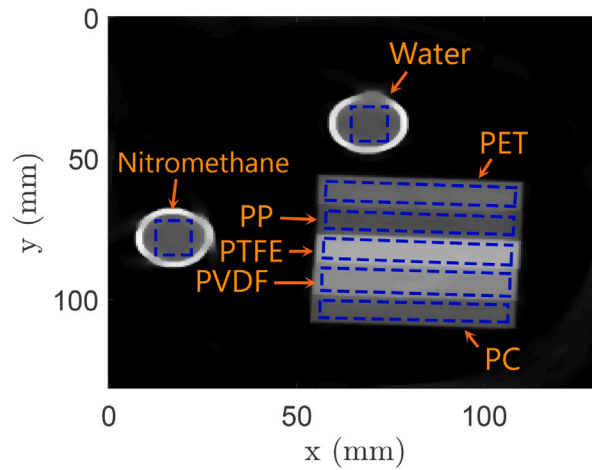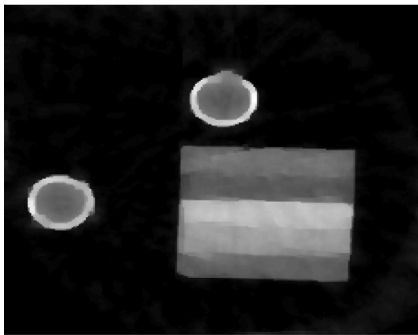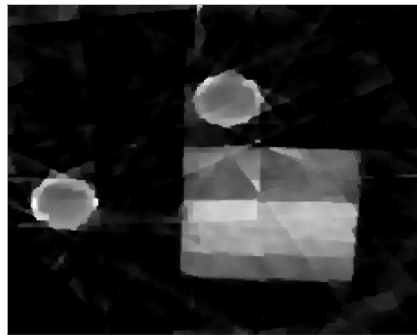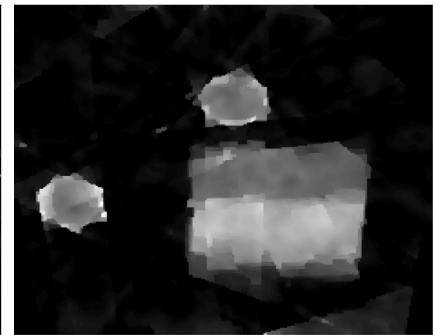
(a) 360 projections, $\lambda = 0.3$

(b) 36 projections, $\lambda = 2.0$ (c) 12 projections, $\lambda = 8.0$ (d) 7 projections, $\lambda = 12.0$

Fig. 6. Reconstructions from different numbers of projections, corresponding to data from the energy bin at 48.7 keV. The polypropylene (PP) material is not included in the classifications because it is contaminated with chemical colorants, resulting in a higher Z_{eff} value than the clean PP. The selected ROIs for each material are indicated by blue dashed lines in the frame (a).

Fig. 6 shows the image reconstructions of the sample performed from different numbers of projections. Even though the reconstruction quality decreases with decreasing number of projections, the mean relative deviation shown in Fig. 5(b) does not decrease. This is because we manually segment the inner materials within the samples by using the reconstructions from 360 projections, and the LACs are then extracted for all numbers of projections. We expect that using an automatic segmentation from 7 projections will significantly reduce the classification performance, since the image edges of different materials in the 7-projection reconstruction are not well preserved. The reconstructions quality in Fig. 6 implies that manual segmentation can be performed from 12 projections, below which the reconstruction quality is significantly deteriorated and it becomes more difficult even for manual segmentation. Therefore, we use just 12 projections for the estimates presented in the subsequent subsections, except for Section 3.5. Using fewer projections enables a faster scan and a lower dose, important for security and medical applications. Note that the weighting parameter used for each reconstruction shown in Fig. 6 was selected based on image quality perceived by human eyes, and can be significantly different from a weighting parameter which gives the optimal results in terms of overall classification performance for all the samples. It is still an unsolved question how to set the optimal weighting parameter automatically, which changes significantly with the type of sample in terms of reconstruction quality and classification performance. Also note that full automatic segmentation of objects in images represents an obvious problem to be solved before industrial implementation, while a manual segmentation scheme is used in this work.

3.3. Classification performance as a function of the number of energy bins used

How a source spectrum is sampled for the cases of 2, 6, 15 and 90 energy bins with and without gaps was described in Section 2.3. In this subsection, since large datasets are processed due to different cases of energy bins rebinning procedures, we use fast image reconstruction algorithm of the FBP. The calibration step was performed using the reference materials listed in Table 1. Fig. 7 shows the relative deviations for Z_{eff} for different numbers of energy bins. The results are shown for all the test materials. In the case of 2 bins, the mean relative deviation decreases from 5.2% to 3.7% when a 8.8-keV-wide gap is introduced. In the case of 6 bins, the mean relative deviation decreases from 2.7% to 2.1% when 8.8-keV-wide gaps are entered. In the case of 15 bins, the deviation increases from 2% to 2.9% when there are gaps of 3.3 keV width between the bins. The case of 90 bins yields the mean relative deviation of 2.6%. Thus, the deviation can be reduced if the width of the input gaps is approximately larger than the intrinsic energy resolution of the detector, assuming a constant energy resolution of 8 keV (FWHM) [57]. When energy gaps were introduced in the 15-bin case, a noticeable increase in deviations was observed instead of a decrease in deviations as in the cases of 2 and 6 bins. We can assume that there are 2 reasons for this finding. First, since the gap widths are smaller than the detector's energy resolution, the bins are still in a state of intersection with each other. Second, the decrease in the number of received photons in bins of reduced width increases the amount of noise in them. This reduces the accuracy in measuring the spectral LACs of materials. This variation in measurement can be particularly
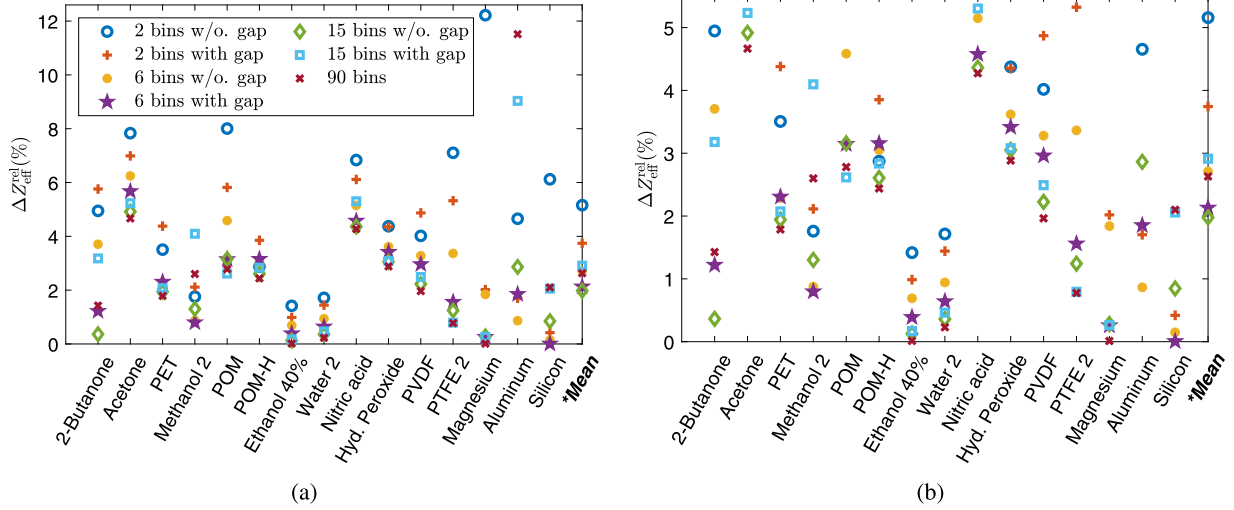
Fig. 7. Plots of Z_{eff} estimation accuracy for all the test materials scanned, obtained with different numbers of energy bins. Note that to show the given values more clearly, a magnified version of the frame (a) is displayed in the frame (b). *The mean deviation was calculated from absolute values of relative deviations for each material. Corrected data collected from 360 projections, and PE and PVC as basis materials, were used to obtain the results presented. The abbreviation w/o. stands for 'without'. The absolute values of relative deviations are shown.

significant at lower energies. This is especially evident for the cases of 15 bins with gaps and 90 bins for aluminum. The 2-bin cases with and without gap give the largest deviations. Hence, the cases of 6 bins with gaps and 15 bins without gaps show almost identical and minimum deviations, and yield no outliers by their large deviations greater than 6%. Considering the computation time, which mainly depends on the image reconstruction step for each energy channel, the case of 6 bins with inter-gaps can be considered as optimal rebinning, as expected. However, in the following sections, we use the 15 bins with no gaps, which performed very slightly better, for our calculations.

3.4. Classification performance as a function of the number of basis materials

The different basis materials used in the classifications are introduced in Table 4. The calibration step was performed using the reference materials listed in Table 1. Fig. 8(a) shows the plots of the relative deviation for Z_{eff} as a function of the weighting parameter λ for different numbers of basis materials in LAC decomposition. The case of 2 basis materials gives the lowest point with deviation of 2.2% (at $\lambda = 60$), while the cases of 5 and 6 basis materials yield the highest points both with same deviations of 4.3% (at $\lambda = 12$). The deviations at the lowest points for the cases of 3 and 4 basis materials are almost the same, with the approximate value of 2.8% (at $\lambda = 40$). Thus, the classification performance decreases with an increased number of basis materials. According to Eq. (3), when the number of basis materials N increases, the BMD model faces more noise challenges to compute a_i magnitudes for the basis materials ($i = 1, 2, \ldots, N$). This finding is also reported in several research papers [73,74].

To experimentally explore the reason behind the performance degradation with increasing number of basis materials in LAC decomposition, the sample illustrated in Fig. 8(c) was scanned with different integration times per projection of the detector such as 2, 10, 50 and 100 ms. The PVC volume fractions are calculated for each basis material decomposition of spectral LACs of the materials within the sample and for each integration time. Fig. 8(b) shows the mean value of the PVC volume fractions from the different integration times and the corresponding maximum deviation from the mean for the different number of basis materials. One observes that the mean value decreases

while the respective maximum deviation increases significantly as the number of basis materials increases for both materials. For PEEK (polyetheretherketone) within the sample (in Fig. 8(c)), the mean value of the PVC volume fractions for each number of basis materials is relatively much smaller than those of aluminum and magnesium 2. The mean value for PEEK with relatively lower Z_{eff} and density values is equal to 1.3×10^{-2} with the maximum deviation of 21% and 0.3×10^{-2} with 38% for 2 and 6 basis materials, respectively. Therefore, the results for this material are excluded in Fig. 8(b). Thus, the use of a higher number of basis materials makes the LAC decomposition more susceptible to noise. Therefore, we use just two basis materials (PE and PVC) for the estimates presented in the other subsections.

3.5. Method comparison

Table 5 lists the relative deviations for different materials obtained from the BMD and SIMCAD methods. The BMD method yields results with an overall mean relative deviation of 3% for Z_{eff} obtained using the approach of 15 energy bins without inter-gaps, while the SIMCAD gives mean deviations of 1.6% for ρ_e and 3.1% for Z_{eff} obtained with optimized bi-energy bins [53]. To be consistent with Ref. [53] in comparing the performance, the 2D reconstructions were carried out from 360 projections with the SIRT in this subsection. The BMD has significantly reduced the Z_{eff} relative deviation for PMMA, PC, POM-H, hydrogen peroxide solution, water and silicon compared to the SIMCAD, however the former has acetone as an outlier with a relative deviation of -7.2%, while the latter shows a deviation of -1% for acetone. Overall, the BMD method shows better robustness for plastics classification, which indicates a higher robustness to the spectral distortions in the measured LACs for plastics.

SIMCAD has the main advantage that it can estimate both material properties, ρ_e and Z_{eff}, suggesting a complete way to distinguish materials. Since this method uses an attenuation decomposition model based on photoelectric absorption and Compton scattering interactions, for which energy-dependent basis functions are smooth and cannot approximate K-edge discontinuities [8], the energy bins below the edge are truncated to make K-edge materials compatible with this method. However, this will limit the energy range, and therefore may decrease the classification performance. The BMD method, on the other hand,
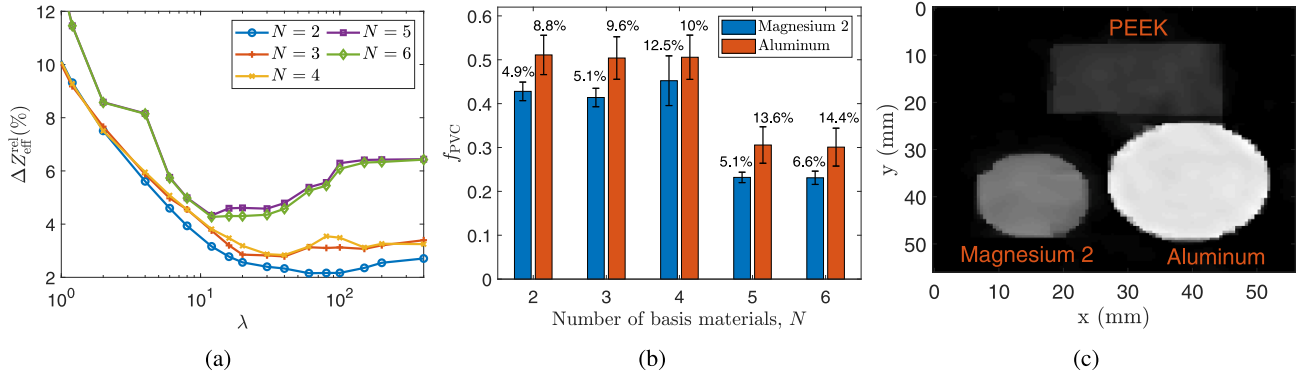
Fig. 8. Investigation of the classification performance with respect to the number of basis materials in LAC decomposition. (a) The relative deviations for Z_{eff} as a function of weighting parameter λ, obtained with different numbers of basis materials N. The plot shows the mean absolute values of relative deviations calculated from the test materials listed in Table 2. Note the logarithmic scale in the x-axis. (b) The mean PVC volume fractions and the corresponding maximum deviations from the mean for the different numbers of basis materials, each calculated from 4 measurements which used integration (acquisition) times of 2, 10, 50 and 100 ms. (c) Image reconstruction of the sample used to obtain the results presented in the frame (b), corresponding to 100 ms and the energy bin at 48.7 keV. Corrected data collected from 12 projections and rebinned into 15 energy bins were used to obtain the results presented.

Table 5
The relative deviations of measured material properties relative to reference values. To compare, values for SIMCAD, another material characterization method using spectral CT data, are taken from Ref. [53]. [a]The mean values are computed from the absolute values of each column.

Material	$Z_{\text{eff}}^{\text{ref}}$	BMD $\Delta Z_{\text{eff}}^{\text{rel}}$(%)	SIMCAD $\Delta Z_{\text{eff}}^{\text{rel}}$(%)	$\rho_{\text{e}}^{\text{ref}}$	SIMCAD $\Delta \rho_{\text{e}}^{\text{rel}}$(%)
PMMA	6.60	1.3	5.1	0.636	−2.0
PTFE	8.50	4.6	4.5	1.035	−2.7
PVDF	8.01	4.1	3.5	0.896	−0.8
PC	6.48	1.0	2.0	0.610	−1.6
POM-C	7.07	3.2	3.6	0.753	−0.6
PET	6.74	1.2	1.1	0.721	−1.4
POM-H	7.07	2.7	5.5	0.763	−2.0
Acetone	6.44	−7.2	−1.0	0.432	1.6
Hyd. Peroxide	7.65	−1.9	4.6	0.661	2.4
Methanol	6.86	−4.5	5.6	0.446	1.1
Water	7.54	−2.6	4.4	0.554	0.5
Nitromethane	7.27	−3.2	−2.3	0.597	2.6
Aluminum	13	3.2	−2.5	1.3	0.9
Silicon	14	−0.1	−1.2	1.161	3.4
Magnesium	12	−3.6	−2.4	0.859	0.03
Mean[a]	–	3.0	3.1	–	1.6

can be used to classify materials with a K-edge in their LACs, as mentioned in the Section 2.5, however none of the materials estimated in this study have a K-edge within the detector's energy region.

4. Conclusion

We have presented the BMD method for material characterization with the physical parameter Z_{eff} using a spectral CT instrument. The results were demonstrated experimentally with a wide range of materials, with focus on security screening applications. The method requires a calibration step employing reference materials, from which Z_{eff} is interpolated or extrapolated through polynomial curve fitting. Correction of the detector's spectral response eliminates significant spectral artifacts from the LAC, and classification even with just two basis materials is demonstrated to require the correction. We explored the classification performance as a function of the number of projections, the number of energy bins and the number of basis materials in LAC decomposition. We found the method to be most accurate employing two basis materials, and 6 energy bins with inter-gaps and 15 bins without gaps. The number of projections for reconstructions can be significantly decreased while image segmentation still can be achieved to extract the LACs and thereby maintain a desired level of classification accuracy. The BMD method shows better robustness to plastic materials than the SIMCAD method in terms of estimating Z_{eff}, even though they give comparable results in mean classification accuracy.

The method presented in this work is thus valid only for Z_{eff} extraction. The Z_{eff} sensitivity alone is not a sufficient parameter for

full classification capability. Complete characterization can be achieved with a (ρ, Z_{eff}) couple since some materials may have noticeably different density values, while having similar Z_{eff} values. However, this method can be employed in the presence of materials with K-edges, where standard techniques are hampered. The optimization procedures of energy bins rebinning and inter-gaps have been presented as a major source of novelty in this paper. Future extensions of this work will focus on investigating materials with K-edges.

For energy-resolving PCDs, there is the need to take energy resolution into account to measure the detector performance. Energy resolution is a key parameter to represent the capability of an energy resolved detector to separate photons in different energy bins. Physical effects in PCDs such as photon pileup, K-fluorescence, charge sharing and cross-talk degrade the energy resolution of the PCDs, decreasing the reliability of the spectral information and leading to a deterioration of material classification accuracy with the BMD. The ability of the imaging system to identify the material composition of the imaged object is generally dependent on energy resolution of the detector [33,35]. Different CdTe spectral detectors, such as Medipix-3 and Pixirad/Pixie-III, have been developed for spectral CT applications. Compared to the detector used in this work, detectors such as Medipix-3 and Pixirad/Pixie-III feature significantly sharper energy resolutions around 3–4 keV FWHM [75,76]. Even though these detectors have a limited number of energy thresholds in the range of 2–8, it is easy to implement different acquisition modes and threshold values. Such detectors are being further developed to enhance energy resolution, which depends on the properties of the CdTe crystal, the source and

the readout electronics, and at the same time to increase the high flux capability. As next steps we also plan measurements with more advanced detectors with sharper energy resolutions, which are expected to potentially improve material classification performance.

CRediT authorship contribution statement

Doniyor Jumanazarov: Conceptualization, Methodology, Software, Formal analysis, Investigation, Data curation, Writing – original draft, Visualization. **Asalkhon Alimova:** Conceptualization, Methodology, Validation, Formal analysis, Investigation, Writing – review & editing. **Azamat Abdikarimov:** Software, Validation, Formal analysis. **Jakeoung Koo:** Software, Validation, Formal analysis. **Henning F. Poulsen:** Writing – review & editing, Supervision. **Ulrik L. Olsen:** Validation, Resources, Data curation, Writing – review & editing, Supervision. **Mihai Iovea:** Validation, Writing – review & editing, Supervision, Funding acquisition.

Declaration of competing interest

The authors declare that they have no known competing financial interests or personal relationships that could have appeared to influence the work reported in this paper.

Data and code availability

The raw and spectral corrected data required to reproduce these findings are available to download from https://doi.org/10.5281/zenodo. 4780625. The developed code for L_∞-TVT joint reconstruction algorithm is available at https://github.com/JuliaTomo/XfromProjections. jl.

Acknowledgments

References

[1] R.C. Chen, R. Longo, L. Rigon, F. Zanconati, A. De Pellegrin, F. Arfelli, D. Dreossi, R.H. Menk, E. Vallazza, T.Q. Xiao, E. Castelli, Measurement of the linear attenuation coefficients of breast tissues by synchrotron radiation computed tomography, Phys. Med. Biol. 55 (17) (2010) 4993–5005.

[2] Z. Qi, J. Zambelli, N. Bevins, G.H. Chen, Quantitative imaging of electron density and effective atomic number using phase contrast CT, Phys. Med. Biol. 55 (9) (2010) 2669–2677.

[3] M.D. Agrawal, D.F. Pinho, N.M. Kulkarni, P.F. Hahn, A.R. Guimaraes, D.V. Sahani, Oncologic applications of dual- energy CT in the abdomen, Radiographics 34 (3) (2014) 589–612.

[4] H.W. Goo, J.M. Goo, Dual-energy CT: New horizon in medical imaging, Korean J. Radiol. 18 (4) (2017) 555–569.

[5] M. Ellenbogen, R. Bijjani, Liquids and homemade explosive detection, in: Optics and Photonics in Global Homeland Security V and Biometric Technology for Human Identification VI, Vol. 7306, International Society for Optics and Photonics, 2009, p. 73060Y, http://dx.doi.org/10.1117/12.821806.

[6] B. De Man, J. Nuyts, P. Dupont, G. Marchal, P. Suetens, Metal streak artifacts in X-ray computed tomography: A simulation study, IEEE Trans. Nucl. Sci. 3 (1999) 1860–1865.

[7] R.A. Brooks, G. Di Chiro, Beam hardening in X-ray reconstructive tomography, Phys. Med. Biol. 21 (3) (1976) 390–398.

[8] R.E. Alvarez, A. Macovski, Energy-selective reconstructions in X-ray computerised tomography, Phys. Med. Biol. 21 (5) (1976) 733–744.

[9] Z. Ying, R. Naidu, C.R. Crawford, Dual energy computed tomography for explosive detection, J. X-Ray Sci. Technol. 14 (4) (2006) 235–256.

[10] S.G. Azevedo, H.E. Martz, M.B. Aufderheide, W.D. Brown, K.M. Champley, J.S. Kallman, G.P. Roberson, D. Schneberk, I.M. Seetho, J.A. Smith, System-independent characterization of materials using dual-energy computed tomography, IEEE Trans. Nucl. Sci. 63 (1) (2016) 341–350.

[11] K.M. Champley, S.G. Azevedo, S. Member, I.M. Seetho, S.M. Glenn, L.D. Mcmichael, J.A. Smith, J.S. Kallman, W.D. Brown, H.E. Martz, Method to extract system-independent material properties from dual-energy X-Ray CT, IEEE Trans. Nucl. Sci. 66 (3) (2019) 674–686.

[12] W.A. Kalender, W. Perman, J. Vetter, E. Klotz, Evaluation of a prototype dual-energy computed tomographic apparatus. I. Phantom studies, Med. Phys. 13 (3) (1986) 334–339.

[13] B.J. Heismann, J. Leppert, K. Stierstorfer, Density and atomic number measurements with spectral X-ray attenuation method, J. Appl. Phys. 94 (3) (2003) 2073–2079.

[14] J.S. Park, J.K. Kim, Calculation of effective atomic number and normal density using a source weighting method in a dual energy X-ray inspection system, J. Korean Phys. Soc. 59 (4) (2011) 2709–2713.

[15] T.P. Szczykutowicz, Z. Qi, G.-H. Chen, A simple image based method for obtaining electron density and atomic number in dual energy CT, in: Medical Imaging 2011: Physics of Medical Imaging, Vol. 7961, International Society for Optics and Photonics, 2011, p. 79613A, http://dx.doi.org/10.1117/12.878076.

[16] O. Semerci, E.L. Miller, A parametric level-set approach to simultaneous object identification and background reconstruction for dual-energy computed tomography, IEEE Trans. Image Process. 21 (5) (2012) 2719–2734.

[17] G. Landry, J. Seco, M. Gaudreault, F. Verhaegen, Deriving effective atomic numbers from DECT based on a parameterization of the ratio of high and low linear attenuation coefficients, Phys. Med. Biol. 58 (19) (2013) 6851–6866.

[18] H.E. Martz, C.M. Logan, D.J. Schneberk, P.J. Shull, X-ray Imaging: Fundamentals, Industrial Techniques and Applications, CRC Press, 2016.

[19] S. Ohira, H. Washio, M. Yagi, T. Karino, K. Nakamura, Y. Ueda, M. Miyazaki, M. Koizumi, T. Teshima, Estimation of electron density, effective atomic number and stopping power ratio using dual-layer computed tomography for radiotherapy treatment planning, Phys. Med. 56 (September) (2018) 34–40.

[20] B. Schmidt, T. Flohr, Principles and applications of dual source CT, Phys. Med. 79 (September) (2020) 36–46.

[21] J. Fornaro, S. Leschka, D. Hibbeln, A. Butler, N. Anderson, G. Pache, H. Scheffel, S. Wildermuth, H. Alkadhi, P. Stolzmann, Dual- and multi-energy CT: approach to functional imaging, Insights Imaging 2 (2) (2011) 149–159.

[22] A.C. Silva, B.G. Morse, A.K. Hara, R.G. Paden, N. Hongo, W. Pavlicek, Dual-energy (spectral) CT: applications in abdominal imaging, Radiographics 31 (4) (2011) 1031–1046.

[23] M. Antoniassi, A.L. Conceição, M.E. Poletti, Study of effective atomic number of breast tissues determined using the elastic to inelastic scattering ratio, Nucl. Instrum. Methods Phys. Res. A 652 (1) (2011) 739–743.

[24] M. Bazalova, E.E. Graves, The importance of tissue segmentation for dose calculations for kilovoltage radiation therapy, Med. Phys. 38 (6) (2011) 3039–3049.

[25] M. Kurudirek, Effective atomic numbers and electron densities of some human tissues and dosimetric materials for mean energies of various radiation sources relevant to radiotherapy and medical applications, Radiat. Phys. Chem. 102 (2014) 139–146.

[26] H. Manjunatha, Comparison of effective atomic numbers of the cancerous and normal kidney tissue, Radiat. Prot. Environ. 38 (3) (2015) 83.

[27] H.C. Manjunatha, L. Seenappa, Pocket formula for mass attenuation coefficient, effective atomic number, and electron density of human tissues, Nucl. Sci. Tech. 30 (3) (2019).

[28] K. Wells, D.A. Bradley, A review of X-ray explosives detection techniques for checked baggage, Appl. Radiat. Isot. 70 (8) (2012) 1729–1746.

[29] P.M. Shikhaliev, Energy-resolved computed tomography: First experimental results, Phys. Med. Biol. 53 (20) (2008) 5595–5613.

[30] A. Brambilla, P. Ouvrier-Buffet, J. Rinkel, G. Gonon, C. Boudou, L. Verger, Cdte linear pixel X-ray detector with enhanced spectrometric performance for high flux X-ray imaging, IEEE Trans. Nucl. Sci. 59 (4 PART 3) (2012) 1552–1558.

[31] X. Wang, D. Meier, K. Taguchi, D.J. Wagenaar, B.E. Patt, E.C. Frey, Material separation in X-ray CT with energy resolved photon-counting detectors, Med. Phys. 38 (3) (2011) 1534–1546.

[32] M.J. Willemink, M. Persson, A. Pourmorteza, N.J. Pelc, D. Fleischmann, Photon-counting CT: Technical principles and clinical prospects, Radiology 289 (2) (2018) 293–312.

[33] S. Leng, M. Bruesewitz, S. Tao, K. Rajendran, A.F. Halaweish, N.G. Campeau, J.G. Fletcher, C.H. McCollough, Photon-counting detector CT: System design and clinical applications of an emerging technology, Radiographics 39 (3) (2019) 729–743.

[34] M. Simard, R.K. Panta, S.T. Bell, A.P. Butler, H. Bouchard, Quantitative imaging performance of MARS spectral photon-counting CT for radiotherapy, Med. Phys. 47 (8) (2020) 3423–3434.

[35] M. Danielsson, M. Persson, M. Sjölin, Photon-counting X-ray detectors for CT, Phys. Med. Biol. 66 (3) (2021) 03TR01.

[36] K. Taguchi, I. Blevis, K. Iniewski, Spectral, Photon Counting Computed Tomography: Technology and Applications, CRC Press, 2020.

[37] M. Joshi, D.A. Langan, D.S. Sahani, A. Kambadakone, S. Aluri, K. Procknow, X. Wu, R. Bhotika, D. Okerlund, N. Kulkarni, D. Xu, Effective atomic number accuracy for kidney stone characterization using spectral CT, in: Medical Imaging 2010: Physics of Medical Imaging, Vol. 7622, No. March 2010, 2010, p. 76223K.

[38] K. Taguchi, J.S. Iwanczyk, Vision 20/20: Single photon counting x-ray detectors in medical imaging., Med. Phys. 40 (10) (2013) 100901.

[39] N.G. Anderson, A.P. Butler, Clinical applications of spectral molecular imaging: Potential and challenges, Contrast Media Mol. Imaging 9 (1) (2014) 3–12.

[40] A. Potop, V. Rebuffel, J. Rinkel, A. Brambilla, F. Peyrin, L. Verger, Investigation of the polynomial approach for material decomposition in spectral X-ray tomography using an energy-resolved detector, in: Medical Imaging 2014: Physics of Medical Imaging, Vol. 9033, No. March 2014, 2014, p. 90333I.

[41] C.O. Schirra, B. Brendel, M.A. Anastasio, E. Roessl, Spectral CT: A technology primer for contrast agent development, Contrast Media Mol. Imaging 9 (1) (2014) 62–70.

[42] P.M. Shikhaliev, Soft tissue imaging with photon counting spectroscopic CT, Phys. Med. Biol. 60 (6) (2015) 2453–2474.

[43] L. Martin, Enhanced Information Extraction in Multi-Energy X-ray Tomography for Security (Ph.D. thesis), Boston University, 2014.

[44] M. Busi, Enhanced Security Screening Using Spectral X-ray Imaging (Ph.D. thesis), Technical University of Denmark, 2019.

[45] V. Rebuffel, J. Rinkel, J. Tabary, L. Verger, New perspectives of X-ray techniques for explosive detection based on CdTe/CdZnTe spectrometric detectors, in: Proc. of the Int. Symp. on Digital Industrial Radiology and Computed Tomography, Vol. 2, 2011, pp. 1–8.

[46] J. Rinkel, G. Beldjoudi, V. Rebuffel, C. Boudou, P. Ouvrier-buffet, G. Gonon, L. Verger, A. Brambilla, Experimental evaluation of material identification methods with CdTe X-ray spectrometric detector, IEEE Trans. Nucl. Sci. 58 (5) (2011) 2371–2377.

[47] G. Beldjoudi, V. Rebuffel, L. Verger, V. Kaftandjian, J. Rinkel, Multidimensional data processing methods for material discrimination using an ideal X-ray spectrometric photon counting detector, IEEE Trans. Nucl. Sci. 58 (6 PART 2) (2011) 3190–3203.

[48] G. Beldjoudi, V. Rebuffel, L. Verger, V. Kaftandjian, J. Rinkel, An optimised method for material identification using a photon counting detector, Nucl. Instrum. Methods Phys. Res. A 663 (1) (2012) 26–36.

[49] R. Alvarez, E. Seppi, A comparison of noise and dose in conventional and energy selective computed tomography, IEEE Trans. Nucl. Sci. 26 (2) (1979) 2853–2856.

[50] S.J. Riederer, C. Mistretta, Selective iodine imaging using K-edge energies in computerized x-ray tomography, Med. Phys. 4 (6) (1977) 474–481.

[51] L. Lehmann, R. Alvarez, A. Macovski, W. Brody, N. Pelc, S.J. Riederer, A. Hall, Generalized image combinations in dual KVP digital radiography, Med. Phys. 8 (5) (1981) 659–667.

[52] A. Brambilla, A. Gorecki, A. Potop, C. Paulus, L. Verger, Basis material decomposition method for material discrimination with a new spectrometric X-ray imaging detector, J. Instrum. 12 (8) (2017) P08014.

[53] D. Jumanazarov, J. Koo, M. Busi, H.F. Poulsen, U.L. Olsen, M. Iovea, System-independent material classification through X-ray attenuation decomposition from spectral X-ray CT, NDT and E International 116 (July) (2020) 102336.

[54] W. Mayneord, The significance of the roentgen, Acta Int. Union Against Cancer 2 (1937) 271.

[55] F.W. Spiers, Effective atomic number and energy absorption in tissues., Br. J. Radiol. 19 (218) (1946) 52–63.

[56] A. Bonnin, P. Duvauchelle, V. Kaftandjian, P. Ponard, Concept of effective atomic number and effective mass density in dual-energy X-ray computed tomography, Nucl. Instrum. Methods Phys. Res. B 318 (PART B) (2014) 223–231.

[57] A. Brambilla, P. Ouvrier-Buffet, G. Gonon, J. Rinkel, V. Moulin, C. Boudou, L. Verger, Fast CdTe and CdZnTe semiconductor detector arrays for spectroscopic X-ray imaging, IEEE Trans. Nucl. Sci. 60 (1) (2013) 408–415.

[58] E.S. Dreier, J. Kehres, M. Khalil, M. Busi, Y. Gu, R. Feidenhans, U.L. Olsen, Spectral correction algorithm for multispectral CdTe X-ray detectors, Opt. Eng. 57 (5) (2018) 16.

[59] S. Kim, J. Chen, T. Cheng, A. Gindulyte, J. He, S. He, Q. Li, B.A. Shoemaker, P.A. Thiessen, B. Yu, L. Zaslavsky, J. Zhang, E.E. Bolton, PubChem 2019 update: Improved access to chemical data, Nucleic Acids Res. 47 (D1) (2019) D1102–D1109, http://dx.doi.org/10.1093/nar/gky1033, URL: https://pubchem.ncbi.nlm.nih.gov.

[60] D. Jumanazarov, J. Koo, H.F. Poulsen, U.L. Olsen, M. Iovea, Significance of the spectral correction of photon counting detector response in material classification from spectral X-ray CT, J. Med. Imaging 9 (3) (2022) 1–24.

[61] M. Berger, J. Hubbell, S. Seltzer, J. Chang, J. Coursey, R. Sukumar, D. Zucker, K. Olsen, XCOM: Photon Cross Section Database, National Institute of Standards and Technology, Gaithersburg, MD, 2010, http://dx.doi.org/10.18434/T48G6X, URL: http://physics.nist.gov/xcom.

[62] D.J. Schroeder, Astronomical Optics, Elsevier, 1999.

[63] J. Gregor, T. Benson, Computational analysis and improvement of SIRT, IEEE Trans. Med. Imaging 27 (7) (2008) 918–924.

[64] D. Jumanazarov, J. Koo, J. Kehres, H.F. Poulsen, U.L. Olsen, M. Iovea, Material classification from sparse spectral X-ray CT using vectorial total variation based on l infinity norm, Mater. Charact. 187 (2022) 111864.

[65] P. Sukovic, N.H. Clinthorne, Penalized weighted least-squares image reconstruction for dual energy X-ray transmission tomography, IEEE Trans. Med. Imaging 19 (11) (2000) 1075–1081.

[66] X. Liu, L. Yu, A.N. Primak, C.H. McCollough, Quantitative imaging of element composition and mass fraction using dual-energy CT: Three-material decomposition, Med. Phys. 36 (5) (2009) 1602–1609.

[67] D. Wu, L. Zhang, X. Zhu, X. Xu, S. Wang, A weighted polynomial based material decomposition method for spectral X-ray CT imaging, Phys. Med. Biol. 61 (10) (2016) 3749–3783.

[68] R.E. Alvarez, Energy dependent information in X-Ray imaging : Part 1 . The vector space description, 1982, unpublished, year.

[69] Shivaramu, Effective atomic numbers for photon energy absorption and photon attenuation of tissues from human organs, Med. Dosim. 27 (1) (2002) 1–9.

[70] M.A. Zenobio, T.A. Silva, M.S. Tavares, E.G. Zenobio, Effective atomic number of human enamel and dentin within a photo energy range from 10 to 200 KeV, ISBN: 9788599141045, 2011.

[71] M.M. Goodsitt, E.G. Christodoulou, S.C. Larson, Accuracies of the synthesized monochromatic CT numbers and effective atomic numbers obtained with a rapid kVp switching dual energy CT scanner, Med. Phys. 38 (4) (2011) 2222–2232.

[72] H.C. Manjunatha, B. Rudraswamy, Study of effective atomic number and electron density for tissues from human organs in the energy range of 1 keV-100 GeV, Health Phys. 104 (2) (2013) 158–162.

[73] B.J. Heismann, B.T. Schmidt, T. Flohr, Spectral Computed Tomography. Chapter 3-Spectral CT Algorithms, SPIE press Bellingham, Wash, 2012, pp. 25–54, http://dx.doi.org/10.1117/3.977546.

[74] V. Di Trapani, L. Brombal, F. Brun, Multi-material spectral photon-counting micro-CT with minimum residual decomposition and self-supervised deep denoising, Opt. Express 30 (24) (2022) 42995–43011.

[75] V. Di Trapani, A. Bravin, F. Brun, D. Dreossi, R. Longo, A. Mittone, L. Rigon, P. Delogu, Characterization of the acquisition modes implemented in Pixirad-1/Pixie-III X-ray detector: Effects of charge sharing correction on spectral resolution and image quality, Nucl. Instrum. Methods Phys. Res. A 955 (May 2019) (2020) 163220.

[76] R. Ballabriga, M. Campbell, X. Llopart, Asic developments for radiation imaging applications: The medipix and timepix family, Nucl. Instrum. Methods Phys. Res. A 878 (July 2017) (2018) 10–23.

Doniyor Jumanazarov is a senior research scientist at the Urgench State University since 2022. He obtained his B.S. degree in physics from the National University of Uzbekistan, Tashkent, Uzbekistan, and his MS degree in Molecular Photonics for bio- and nanotechnologies (MONABIPHOT) from the École Normale Supérieure de Cachan, Cachan, France, in 2012 and 2018, respectively. He was awarded his PhD degree from the Department of Physics at Denmark Technical University (DTU), Kongens Lyngby, Denmark, in 2022. Doniyor's current research interest is the enhancement of image reconstruction and material classification from spectral X-ray CT for industrial applications.

Asalkhon Alimova has obtained her B.S. and M.S. degrees in physics from the National University of Uzbekistan, Tashkent, Uzbekistan, in 2019 and 2021, respectively. Her research interests include X-ray tomography, X-ray imaging and image processing.

Azamat Abdikarimov is a senior research scientist at the Urgench State University since 2007. He was awarded his Ph.D. degree in Physics in 2021 from the Urgench State University. Azamat's current research interest is modeling of semiconductor devices and solar cells.
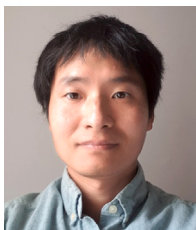
JaKeoung Koo received his B.Sc. and M.Sc. in Computer Science from Chung-Ang University, South Korea in 2015 and 2017, respectively. He was awarded his Ph.D. degree in 2021 from the Technical University of Denmark. He was a Postdoc at Heriot-Watt University, Edinburgh, U.K in 2021 and at National University of Singapore in 2022. He is currently an Assistant Professor at Gachon University, Seoul, South Korea. His research interests include computational imaging, image processing, and geometry processing.

Dr. Ulrik Lund Olsen is a senior research engineer at DTU Physics since 2013. He obtained his Ph.D. degree in 2009 from Copenhagen University. He is an expert in X-ray instrumentation and specializes in spectral X-ray detectors, data acquisition and processing. Ulrik's current research interest is the use of spectral detectors for security applications for improved reconstruction and material identification.

Professor, Dr. techn. Henning Friis Poulsen is employed at DTU Physics since 2012. Henning pioneered several X-ray microscopy methods enabling multiscale mapping of materials properties from the macroscopic and down to nanometre length scales. He heads the 3D Imaging Centre at DTU and is Principal Investigator on a number of European and national projects with the aim of introducing X-ray methods to industry.

Mihai Iovea, Engineer in Physics, Senior Research Scientist, Ph.D in Physics. He has over 30 years' experience in X-ray Imaging projects research & development for Security and Non-Destructive Testing. Interested in X-ray 2D&3D Tomography and Digital Radiography techniques, such as: dual/multi energy, diffraction, back-scattering applied in for threats detection, high-resolution in-line X-ray scanners for fast industrial non-destructive testing.